Geochimica et Cosmochimica Acta 376 (2024) 14–24

Contents lists available at ScienceDirect

Geochimica et Cosmochimica Acta

journal homepage: www.elsevier.com/locate/gca

Hydrological dynamics and manganese mineralization in the wake of the Sturtian glaciation

Yuntao Ye [a,b], Xiaomei Wang [a,*], Huajian Wang [a], Haifeng Fan [c,d], Zhigang Chen [e], Qingjun Guo [d,f], Ziteng Wang [d,f], Chaodong Wu [b], Donald E. Canfield [a,g], Shuichang Zhang [a]

[a] Key Laboratory of Petroleum Geochemistry, Research Institute of Petroleum Exploration and Development, China National Petroleum Corporation, Beijing 100083, China
[b] Key Laboratory of Orogenic Belts and Crustal Evolution, Ministry of Education, School of Earth and Space Sciences, Peking University, Beijing 100871, China
[c] State Key Laboratory of Ore Deposit Geochemistry, Institute of Geochemistry, Chinese Academy of Sciences, Guiyang 550081, China
[d] University of Chinese Academy of Sciences, Beijing 100049, China
[e] College of Ocean and Earth Sciences, Xiamen University, Xiamen 361102, China
[f] Institute of Geographic Sciences and Natural Resources Research, Chinese Academy of Sciences, Beijing 100101, China
[g] Nordcee, Department of Biology, University of Southern Denmark, 5230 Odense, Denmark

ARTICLE INFO

Associate editor: Ruth Blake

Keywords:
Mn carbonate
Rare earth elements
Phosphate oxygen isotopes
Datangpo formation
South China

ABSTRACT

The Cryogenian Sturtian and Marinoan glaciations stand as the most extreme climate events in Earth history. Intriguingly, large-scale Mn carbonates characterize the nonglacial interlude of this period in South China. The formation mechanism of Mn carbonates and the potential correlation underlying this temporal association remain elusive. Here, we present an integrated petrographic and geochemical study of drill core materials intercepting the Mn-bearing Datangpo Formation. Rare earth element patterns of these Mn carbonates exhibit positive Ce anomalies and a lack of Y anomalies, which differ from those of modern seawater but resemble marine Mn-Fe oxides. These features, combined with negative carbonate carbon isotope compositions ($\delta^{13}C_{carb}$ as light as −9.9 ‰ VPDB), indicate the presence of oxide precursors and the incorporation of light carbon during Mn-carbonate precipitation. Phosphate oxygen isotope ratios ($\delta^{18}O_p$) of HCl-extractable apatite reveal a ~4 ‰ difference in the average $\delta^{18}O_p$ between Mn-rich and Mn-poor rocks. We propose that the more positive $\delta^{18}O_p$ of Mn-rich samples may result from the dominance of phosphate released by reductive dissolution of metal oxides or a heavier oxygen isotope signal of surrounding waters with which isotopic equilibrium has been reached. We further illustrate how marine invasions into coastal anoxic basins could have triggered the formation of Mn oxides and highlight the role of glaciation–deglaciation in the development of giant Mn deposits.

1. Introduction

The Cryogenian Period witnessed some of the most intense and long-lived glaciations over geological history, namely the Sturtian and Marinoan Snowball Earth events. During these events, ice sheets probably extended to equatorial regions due to runaway ice–albedo feedback, leading to a near-complete shutdown of the hydrological cycle (Kirschvink, 1992; Hoffman et al., 2017). Deglaciation of the Snowball Earth was achieved as soon as atmospheric CO_2 levels reached a threshold (Hoffman and Schrag, 2002; Shields, 2005). Strikingly, the corresponding injection of glacial meltwater could have affected not only the development of certain deposits but also contemporaneous ecosystems, such as the competition between cyanobacteria and eukaryotic algae (van Maldegem et al., 2019). Recent studies have unveiled evidence of mixing between seawater and freshwater in post-Marinoan sediments (Ahm et al., 2019; Wang et al., 2023a). However, it remains unclear whether a similar scenario occurred after the Sturtian glaciation.

In South China, the Sturtian glacial diamictite is overlaid by a unit of black shales with Mn carbonate interlayers. Although the influence of meltwater on these post-Sturtian sediments is unexplored, numerous studies have been carried out regarding the mineralization pathway of Mn carbonates. Some research attributed the formation of Mn carbonates to the reduction of Mn oxides within anoxic pore waters (Yu et al., 2016, 2017), yet others indicated direct Mn-carbonate precipitation in the water column (Cheng et al., 2021; Ai et al., 2023). In the former case,

* Corresponding author.
E-mail address: wxm01@petrochina.com.cn (X. Wang).

https://doi.org/10.1016/j.gca.2024.05.021
Received 1 March 2023; Accepted 20 May 2024
Available online 25 May 2024

episodic ventilation of anoxic basins would be necessary to account for the accumulation of Mn oxides, aligning with isotopic fractionations driven by the presence of oxide minerals (Zhang et al., 2015; Liu et al., 2023). The direct precipitation hypothesis is largely inspired by the supersaturation of rhodochrosite in modern lakes (Herndon et al., 2018; Wittkop et al., 2020). It is important to note that without comprehensive examination, uncertainties may arise when comparing modern and ancient sediments.

Here, we employ multiple proxies including phosphate oxygen isotopes ($\delta^{18}O_p$), major and trace elements, as well as carbonate carbon isotope compositions ($\delta^{13}C_{carb}$) to provide insights into Mn cycling and hydrological conditions after the Sturtian glaciation. Oxygen isotopes have long been recognized for their utility in monitoring climate and ice volume variations (Grossman and Joachimski, 2022). However, the preservation of primary oxygen isotope signature is not equally reliable across all geological archives. For instance, carbonate oxygen isotopes are known to be vulnerable to diagenetic and meteoric alterations, which can compromise the derived results (Knauth and Kennedy, 2009). In contrast, under abiotic environments of typical marine temperature and pH ranges, phosphate resists oxygen isotope exchange with ambient fluids (Lecuyer et al., 1999; Chang et al., 2021), making $\delta^{18}O_p$ a robust indicator for our research purposes.

2. Geological setting and samples

The South China block was formed through the assembly of the Yangtze and Cathaysia blocks at 980–820 Ma (Fig. 1a). After that, intracontinental rifting took place, generating bimodal volcanism and rift basins that were subsequently filled by Neoproterozoic sediments (Wang and Li, 2003; Shu et al., 2021). The rift–drift transition occurred during the Cryogenian Period. Two diamictite intervals corresponding to the Sturtian and Marinoan glaciations, respectively, have been well documented, and are separated by a nonglacial interlude, dubbed the Datangpo Formation (Jiang et al., 2011; Li et al., 2012). We collected the Datangpo samples from two drill cores (DT1 and DT2) in northeastern Guizhou Province. Paleogeographic reconstruction of this region reveals the existence of a series of NE-SW-trending horsts and grabens (Fig. 1b; Yu et al., 2016, 2017). The Datangpo Formation here can be divided into two members (Fig. 1c and d). Member I is black shales interbedded with Mn carbonates, while in shallow water sections, the Mn carbonate is replaced by dolostone. Member II refers to thick-bedded siltstone. Notably, substantial Mn enrichments are mainly located in the centers of grabens. Zircon U–Pb ages of 658.8 ± 0.5 Ma from the basal Datangpo Formation (Zhou et al., 2019) and 657.2 ± 0.8 Ma from the middle of Member II (Rooney et al., 2020) constrain a maximum duration of 1.6 Ma for Member I deposition (Fig. 1c).

For geochemical measurements, 11 and 50 samples belonging to

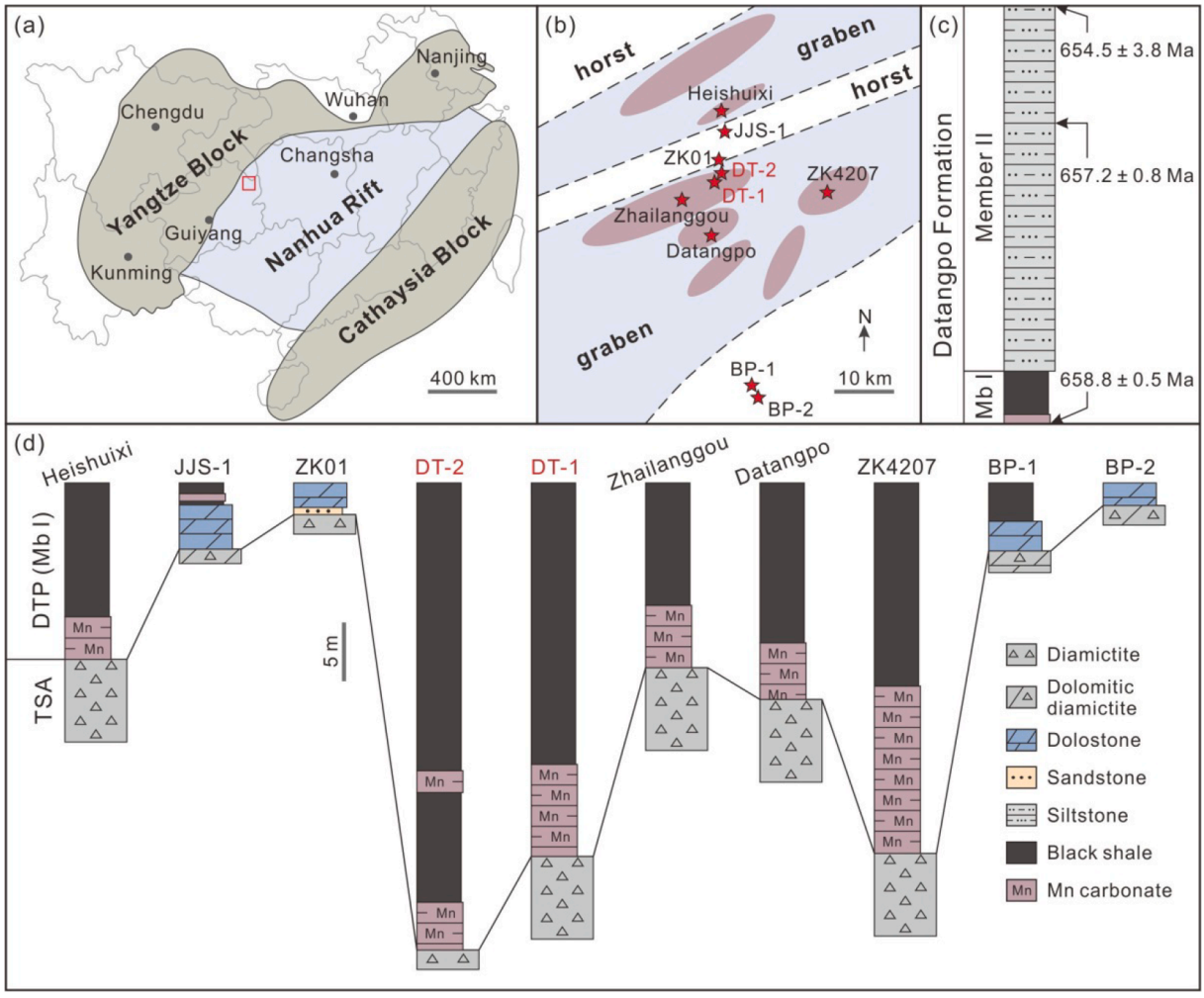

Fig. 1. (a) Tectonic outline of the South China craton. The red rectangle marks the studied area. (b) Paleogeographic map of the studied area (after Yu et al., 2017). (c) Lithostratigraphy of the Datangpo Formation. Age constraints are from Zhang et al. (2008), Zhou et al. (2019), and Rooney et al. (2020). (d) Stratigraphy correlation of the lower Datangpo Formation (Member I). Profiles other than the DT1 and DT2 cores are modified from Yu et al. (2017). TSA, Tiesi'ao Formation; DTP, Datangpo Formation.

Member I of the Datangpo Formation were obtained from the DT1 and DT2 cores, respectively. Phosphate oxygen isotope compositions were determined for 11 samples, including 5 Mn carbonates and 6 Mn-poor shales. Two Mn-carbonate hand specimens were micro-drilled for additional trace element analysis.

3. Methods

Elemental mapping was performed on thin sections with a Bruker M4 TORNADO micro-X-ray fluorescence (μ-XRF) spectrometer at the Key Laboratory of Petroleum Geochemistry (KLPG), China National Petroleum Corporation (CNPC). The relative contents of elements are illustrated as false-color plots. Micro-scale imaging and analysis were determined using a Thermo Fisher Scientific Apreo scanning electron microscope (SEM) equipped with a Bruker XFlash 6–30 energy dispersive spectrometry (EDS). Mineralogical determination via the QEMSCAN mode of operation enables automated pixel-by-pixel spectral acquisition. The elemental composition was compared with mineral databases to generate mineral distribution in areas of interest.

For total organic carbon (TOC) analysis, powdered samples were treated with 5 % HCl at 85 °C to remove carbonate, washed with deionized water, and dried. TOC values were examined by a LECO CS-230HC C-S analyzer at the KLPG, CNPC.

Major element concentrations were determined at the Analytical Laboratory of Beijing Research Institute of Uranium Geology, China National Nuclear Corporation. Fused discs were prepared in a crucible (95 % Pt–5 % Au) with 0.7 g of powdered sample, 5.9 g of flux ($Li_2B_4O_7$–LiF–NH_4NO_3), and 1 mL of LiBr, and melted under 1150–1250 °C for 10–15 min. Discs were analyzed by a PANalytical Axios^{mAX} wavelength dispersive XRF spectrometer. The analytical precision was better than 5 %. For trace element analysis, 40 mg of sample powder was digested in a HNO_3–HF (1:4) acid mixture and kept in the oven at 185 °C for 3 days. After complete digestion and acid evaporation, the sample was diluted with a 2 % HNO_3 solution. Internal spikes of Rh, In, and Re were added. Trace element measurements were conducted by a Thermo Fisher Scientific X Series 2 inductively coupled plasma-mass spectrometer (ICP-MS) at the Guizhou Tongwei Analytical Technology Co., Ltd (GTAT). Analyses of samples and reference materials yielded a precision of better than 10 %. The abundances of rare earth elements were normalized to the Post-Archean Average Shale (PAAS; Taylor and McLennan, 1985) and the ratios of Ce/Ce* and Eu/Eu* were calculated following the equations below (Lawrence et al., 2006):

$$Ce/Ce^* = Ce_N/(Pr_N \times Pr_N/Nd_N) \quad (1)$$

$$Eu/Eu^* = Eu_N/\sqrt{(Sm_N \times Gd_N)} \quad (2)$$

Similarly, the Y anomaly (expressed as Y_N/Ho_N) was determined by normalizing the contents of Y and Ho to PAAS, which allows for a standardized comparison of these elements in a given sample.

Carbonate carbon isotopes were determined for samples with Mn > 1 wt% using a Thermo Fisher Scientific GasBench II linked to a Delta V Plus isotope ratio mass spectrometer (IRMS) at the Institute of Geology and Geophysics, Chinese Academy of Sciences. The sample was reacted with H_3PO_4 at 72 °C for 1 h. The generated CO_2 was purified by passing through two Nafion water traps and a PoraPlot Q chromatography column and introduced into the IRMS system. Carbonate carbon isotopes are reported relative to the Vienna Pee Dee Belemnite (VPDB) standard. The analytical precision of $\delta^{13}C_{carb}$ was better than 0.1 ‰.

A recent P speciation study showed that apatite P (including detrital and authigenic apatite) accounts for ~95 % of the total P pool in the Datangpo Formation, while the amounts of organic P and Fe oxide-bound P are negligible (Bowyer et al., 2023). Therefore, to target the apatite phase, we extracted phosphate using 1 M HCl. Sample powders of 3–10 g were reacted with 1 M HCl (50 ml per gram of sample) on a reciprocal shaker for 16 h. Then, the supernatant was separated from the residue by centrifugation. An aliquot of the supernatant was measured for P content by ICP-MS at the GTAT. Magnesium-induced co-precipitation was utilized to obtain phosphate. The precipitate was dissolved with 10 M HNO_3 and purified by sequential precipitation of phosphate as ammonium phosphomolybdate and magnesium ammonium phosphate. After re-dissolution, the solution was treated with cation resin (AG 50 W-X8, BIO-RAD) first and then anion resin (AG 1-X8, BIO-RAD) to remove interfering ions. Phosphate adsorbed on the anion resin was eluted with 0.2 M $NaHCO_3$. Residual carbonate was removed by 7 M HNO_3 and purging with N_2. The purified phosphate was converted to Ag_3PO_4 by ammonia volatilization. Bright yellow Ag_3PO_4 crystals were obtained without any co-precipitation of other salts. About 0.4–0.8 mg Ag_3PO_4 was used to determine the $\delta^{18}O_p$ ratio by a high-temperature conversion-IRMS (Delta V Advantage, Thermo Fisher Scientific). Measurements were conducted at the College of Ocean and Earth Sciences, Xiamen University according to the method of Chen et al. (2015). The results were reported relative to the Vienna Standard Mean Ocean Water (VSMOW). Standard materials including the B2207 silver phosphate ($\delta^{18}O_p$ = 21.7 ‰, Elemental Microanalysis), the IAEA-601 benzoic acid ($\delta^{18}O$ = 23.14 ‰), and the NBS-127 barium sulfate ($\delta^{18}O$ = 9.3 ‰) were used for calibration. The analytical reproducibility was better than 0.3 ‰. Parallel $\delta^{18}O_p$ analysis was carried out at the Institute of Geographic Sciences and Natural Resources Research, Chinese Academy of Sciences with method described in Wang et al., (2023b). Replicate determinations between the two laboratories agreed within 0.6 ‰.

4. Results

Manganese occurs as laminated (Fig. 2a) or massive (Fig. 2b) carbonate in lower Member I of the Datangpo Formation. SEM images show that Mn-carbonates exhibit globule morphologies with an average diameter of ~5 μm (Fig. 3). Their elemental compositions deviate from the ideal stoichiometry of rhodochrosite ($MnCO_3$), and are referred to as Ca-rhodochrosite hereafter. The intergranular spaces are filled by carbonate cements/overgrowths possessing lower Mn/Ca ratios. By QEMSCAN analysis, we discern alternating laminations of coarse- and fine-grained clastics. The coarse-grained layers mainly consist of quartz and albite that are sub-rounded or sub-angular in shape (Fig. 4a). Ca-rhodochrosite is dominantly enriched within coarse-grained layers, but absent in fine-grained counterparts. On the other hand, in samples with extremely high Mn contents, substantial Ca-rhodochrosite exists with negligible fingerprint of detrital particles (Fig. 4b).

Apatite was detected in either euhedral form (Fig. 5a and b) or as amorphous patches (Fig. 5c and d). Intriguingly, in several samples, we identified rounded apatite cores that are enveloped by secondary overgrowths (Fig. 5e and f). As depicted in Fig. 5, pyrite framboids are also common through SEM observations.

Geochemical analysis delineates multiple intervals of Mn enrichments in Member I (Fig. 6). These Mn-rich samples house moderately positive anomalies of Ce (Ce/Ce* = 0.9–1.4) and Eu (Eu/Eu* = 0.8–1.5) as well as muted Y anomalies (Y_N/Ho_N = 0.9–1.1; Figs. 2 and 7). For samples with Mn > 1 wt%, the Mn contents display positive relationships with Ce/Ce* (R^2 = 0.78; Fig. 7a) and Eu/Eu* (R^2 = 0.68; Fig. 7b), while a negative correlation is seen with $\delta^{13}C_{carb}$ (R^2 = 0.52; Fig. 7c). The $\delta^{18}O_p$ ratios of 1 M HCl leachates from core DT2 show significant fluctuations, spanning from 8.7 ‰ to 16.3 ‰ (Fig. 6). Elevated $\delta^{18}O_p$ is essentially accompanied by high Mn content, and vice versa. Organic matter is abundant in the Datangpo black shales (TOC = 0.75–4.72 wt%) with a decreasing trend up-section (Fig. 6).

5. Discussion

5.1. The origin of the Datangpo Mn carbonate

It is controversial whether Mn carbonates in ancient rocks are the product of diagenetic Mn-oxide reduction (Calvert and Pedersen, 1996;

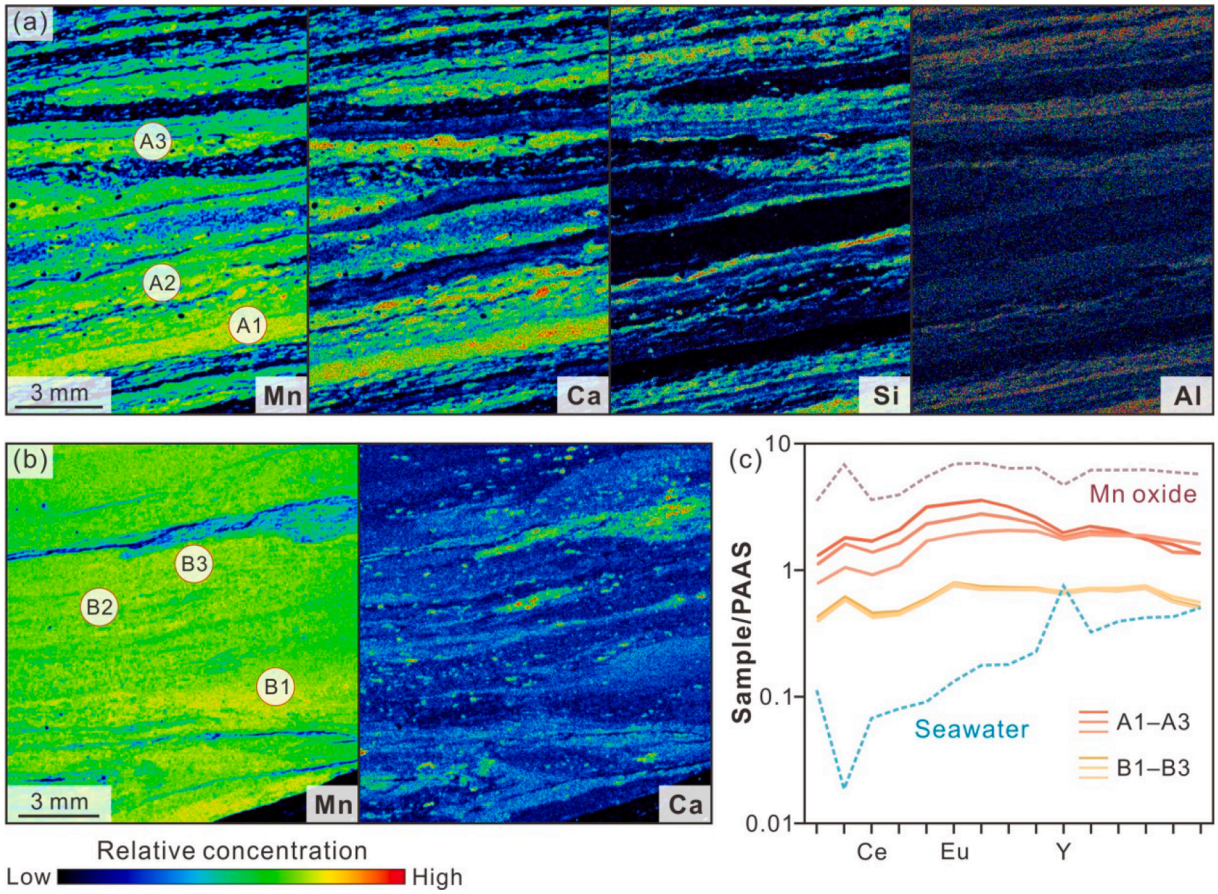

Fig. 2. (a) Micro-XRF elemental imaging of sample DT2-A, depth 1427.9 m. The labeled dots delineate micro-drilled sampling locations. (b) Micro-XRF mapping of sample DT1-B, depth 1317.5 m. (c) PAAS-normalized REE + Y patterns of seawater ($\times 10^6$; Zhang and Nozaki, 1996), marine Mn oxides (Bau et al., 2014), and micro-drilled holes in (a) and (b).

Neumann et al., 1997; Yan et al., 2022; Dong et al., 2023) or direct precipitation from seawater (Havig et al., 2015; Lenz et al., 2015; Herndon et al., 2018; Wittkop et al., 2020). The nature of these compounds as carbonate or oxide depends on water chemistry and redox conditions, with each precipitate carrying its own geochemical signature. Rare earth elements plus Y (REE + Y) have been proven to be useful in quantifying this issue (Bau et al., 2014; Wu et al., 2016; Tostevin et al., 2016; Xiao et al., 2017). Specifically, the Ce anomaly can provide valuable information on depositional redox states. In oxygenated settings, Ce^{3+} is partially oxidized to insoluble Ce^{4+} on the surface of Fe-Mn oxides, inducing positive Ce anomalies in oxide particles and negative Ce anomalies in solutions (Koeppenkastrop and De Carlo, 1992; Zhang and Nozaki, 1996). Similarly, the ratios of Y_N/Ho_N are also sensitive to the presence of Fe-Mn oxides. Compared with Y, Ho is preferentially scavenged onto oxide surfaces. The removal of Ho produces positive Y anomalies in seawater, whereas Fe-Mn oxides typically have Y_N/Ho_N ratios close to or below unity (Bau et al., 2014).

Carbonate rocks precipitated from the water column record seawater-like distribution of REE + Y. For example, the Ediacaran Gaoyan Mn carbonates exhibit strong positive Y anomalies that are thought to reflect direct nucleation of rhodochrosite in seawater (Gao et al., 2021). As depicted in Fig. 2, the REE + Y patterns of the Datangpo Mn carbonates resemble those of marine metal oxides but differ strikingly from seawater. We suggest that the positive Ce anomalies and the lack of Y anomalies point to the inheritance of REE + Y from Mn-oxide precursors, which were subsequently reduced to Mn^{2+} and fixed as carbonates. Notably, the magnitudes of Ce and Y anomalies in the Datangpo samples are less pronounced relative to those found in modern Mn oxides. Because of the slow reaction kinetics of Ce^{3+} oxidation, large positive Ce anomalies are observed in modern Mn crusts with very slow growth rates (a few millimeters per million years; Bau et al., 2014). Hence, Mn accumulation during the Datangpo deposition might have occurred at higher rates than its present-day counterparts. Additionally, the positive correlation between Mn concentrations and Eu/Eu*, an indicator of hydrothermal activity (Sverjensky, 1984), suggests that the development of Mn precipitate could have been limited by hydrothermal Mn supply (Fig. 7b). However, modern hydrogenetic Fe-Mn deposits can also display a subtle positive Eu anomaly due to the enrichment of middle REE (Bau et al., 2014). Hence, the Eu anomalies in our samples do not necessarily align with a hydrothermal origin and the positive relationship could stem from the dilution of detrital materials possessing flat REE signals.

The diagenetic formation of Mn carbonate from Mn oxide is supported by the $\delta^{13}C_{carb}$ data (Fig. 7c). Carbonates depleted in ^{13}C are commonly attributed to the incorporation of carbon generated by organic matter degradation (Neumann et al., 2002; Roy, 2006; Maynard, 2010). Dolostones deposited at shallow sites equivalent to the Datangpo Mn carbonates yield a mean $\delta^{13}C_{carb}$ of −0.9 ‰ (Yu et al., 2017). We take this value to represent coeval seawater composition. In contrast, the minimum $\delta^{13}C_{carb}$ of Mn carbonates is −9.9 ‰, indicating significant contributions from pore-water bicarbonate with a much reduced $\delta^{13}C$ (the $\delta^{13}C_{org}$ ratios are between −34 ‰ and −32.5 ‰ in the zone of Mn enrichments; Ye et al., 2024b; Fig. 6). Due to diffusive exchange with seawater, it is implausible to precisely determine the $\delta^{13}C$ of pore-water bicarbonate from which the Ca-rhodochrosite was precipitated, but our results agree with Mn-oxide deposition to the basin floor followed by diagenetic Mn reduction and Mn-carbonate formation.

Might some Mn carbonates stem from the water column? Direct Mn-

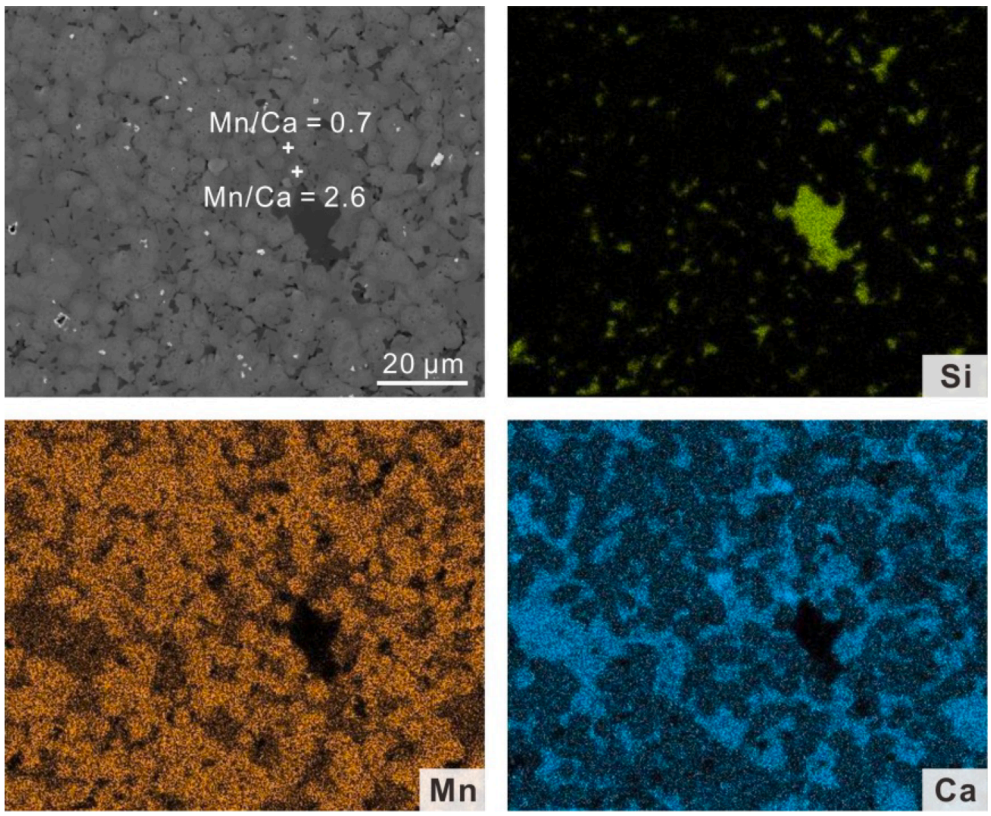

Fig. 3. Backscattered electron photograph and elemental mapping of Mn carbonate. The ratios of Mn/Ca were acquired by EDS analysis.

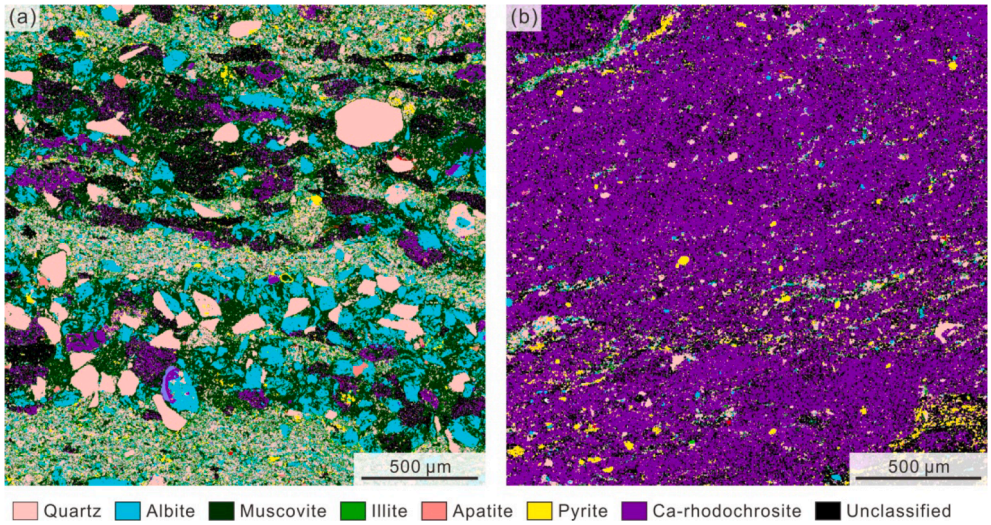

Fig. 4. Representative QEMSCAN results of the Datangpo samples. (a) Alternating laminations of coarse- and fine-grained sediments. (b) Substantial enrichment of Ca-rhodochrosite.

carbonate nucleation has been inferred to take place in modern lakes (Havig et al., 2015; Herndon et al., 2018; Wittkop et al., 2020). A crucial piece of evidence corroborating this process is the zonation of Mn particles, where calcites served as nucleation sites for Mn^{2+} to precipitate, forming discernable Mn-rich rims around calcite cores (Havig et al., 2015; Herndon et al., 2018). However, the Datangpo Mn globules exhibit higher ratios of Mn/Ca (2.6) compared with intergranular cement (0.7; Fig. 3). Such a feature differs from the notion of a preexisting core and challenges the direct precipitation pathway. Notably, throughout our petrographic observation, no relics of Mn oxide were detected, plausibly because of the high organic matter contents in the Datangpo samples, which have facilitated quantitative reduction of Mn oxides.

5.2. *Dynamic hydrological conditions after the Sturtian glaciation*

Our QEMSCAN results reveal two modes of Mn occurrence that can be attributed to varied Mn-oxide sources. The alternating layers of coarse- and fine-grained sediments in Fig. 4a depict the impact of debris flows disrupting a background of suspension fallout. Ca-rhodochrosite is predominantly found within the debris zones but not in the mud layers. We suggest that Mn oxides might be introduced by debris discharge and

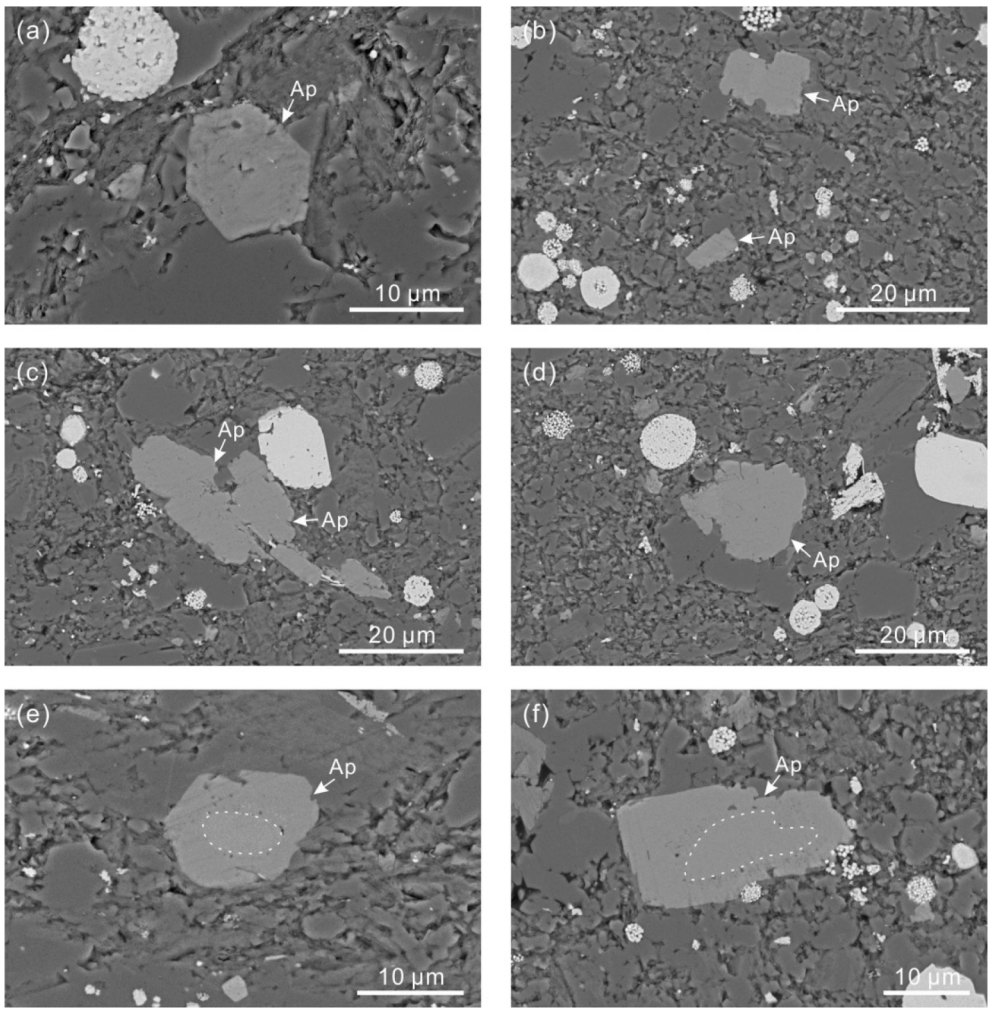

Fig. 5. Backscattered electron photographs of apatite from the lower Datangpo Formation. (a–b) Euhedral crystals. (c–d) Amorphous apatite patches. (e–f) Detrital apatite grains (dashed lines) enveloped by diagenetic overgrowths. Ap, apatite.

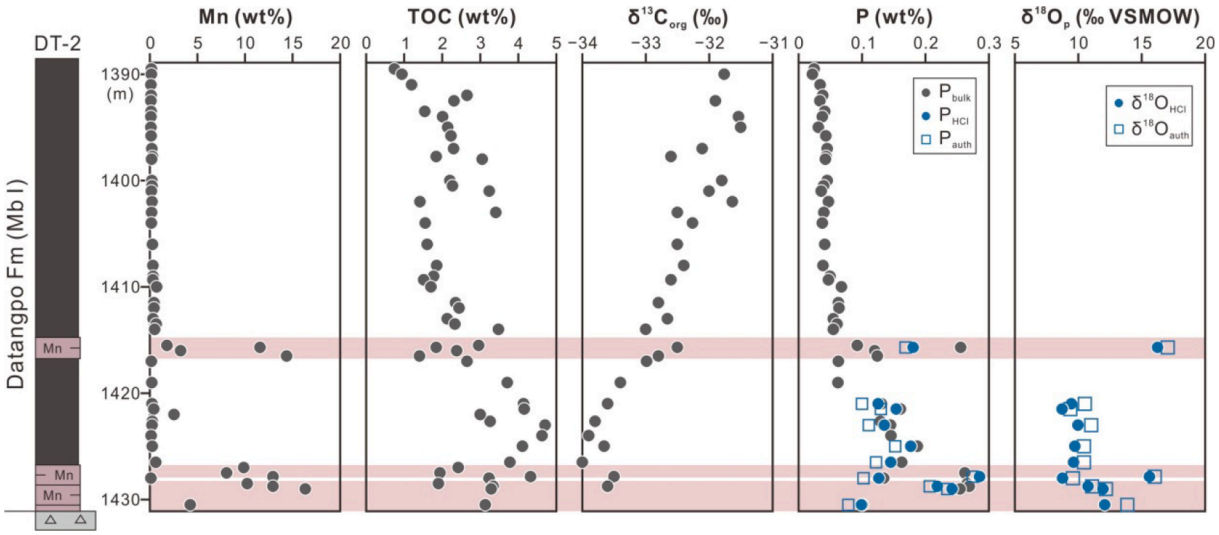

Fig. 6. Geochemistry of the DT2 core, with Mn-rich intervals highlighted in pink. The phosphate oxygen isotope ratios of 1 M HCl leachates ($\delta^{18}O_{HCl}$) and the calculated authigenic values ($\delta^{18}O_{auth}$) are represented by dots and squares, respectively. Profiles of Mn and TOC contents include data from Ye et al. (2018) and this study. Organic carbon isotope compositions ($\delta^{13}C_{org}$) are from Ye et al., (2024b).

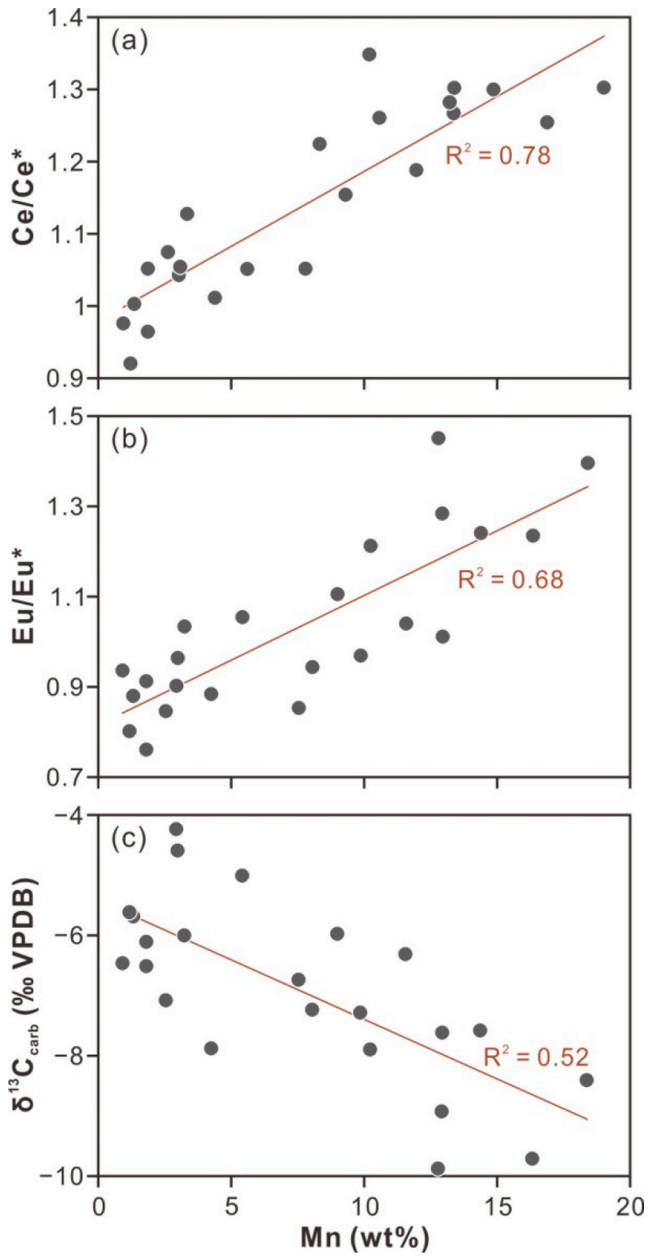

Fig. 7. Cross-plots of Mn contents versus (a) Ce/Ce*, (b) Eu/Eu*, and (c) $\delta^{13}C_{carb}$. Note that the cross-plots include data from both the DT1 and DT2 cores.

undergo reduction to their carbonate form via diagenesis. This type of Mn mineralization, however, is not volumetrically significant due to the relatively small proportions of Mn in these samples. Instances of substantial Mn enrichments occur without any evidence of debris flow (Fig. 4b), indicating an alternative pathway for Mn oxide precipitation. In the following, we explore the possible cause of widespread Mn^{2+} oxidation and why Mn carbonates are associated with the Sturtian glaciation. To do this, we use the $\delta^{18}O_p$ proxy that can provide powerful constraints on paleo-environments (e.g., Liang and Blake, 2007; Blake et al., 2010; Jaisi and Blake, 2010; Goldhammer et al., 2011; McLaughlin et al., 2013; Zhao et al., 2021; Ye et al., 2024a). The P–O bound is very stable under most abiotic conditions but can be rapidly split through enzyme-mediated hydrolysis (Blake et al., 2005; Chang et al., 2021). In particular, the activity of inorganic pyrophosphatase, a ubiquitous intracellular enzyme across all three domains of life, can impose reversible phosphate–water oxygen isotope exchanges, leading to a temperature-dependent equilibrium fractionation (Chang and Blake, 2015):

$$1000 \times \ln\alpha_{p-w} = (14.43 \pm 0.39) \times 1000/T - (26.54 \pm 1.33) \quad (3)$$

$$\alpha_{p-w} = ({}^{18}O/{}^{16}O)_p/({}^{18}O/{}^{16}O)_w = (\delta^{18}O_p + 1000)/(\delta^{18}O_w + 1000) \quad (4)$$

where $({}^{18}O/{}^{16}O)_p$ and $({}^{18}O/{}^{16}O)_w$ denote the ratios of heavy to light oxygen isotopes in phosphate and water, respectively, $\delta^{18}O_w$ is the standard delta value of water oxygen isotopes, and T is the temperature in Kelvin.

Theoretically, phosphate can be preserved in various pools of sedimentary rocks, including loosely sorbed P, metal oxide-bound P, authigenic/biogenic P, detrital P, and organic P (Ruttenberg, 1992). While our research did not involve sequential P extraction to differentiate these P phases, a recent investigation on a Datangpo core (ZK102) adjacent to our sections revealed that ~95 % of the total P reservoir is composed of apatite P (Bowyer et al., 2023). Considering the absence of phosphatic fossils in the Datangpo Formation, our HCl-extractable P mainly represents a mixture of detrital and authigenic apatite. The precipitation of authigenic apatite takes place in the water column or mostly near the sediment–water interface (Paytan et al., 2003; Faul et al., 2005). In environments with heavy organic loading, early diagenetic phosphogenesis could be very active due to the degradation of organic matter and redox cycling of Mn-Fe oxides (Ruttenberg, 2014), which aligns with the observation of apatite overgrowths in our samples (Fig. 5c and d). Experimental results indicated only a small fractionation (~1‰) between authigenic apatite and dissolved phosphate during apatite precipitation (Liang and Blake, 2007). Ideally, the detrital and authigenic P pools should be separated by adding a 1 M acetate extraction step to target authigneic P before the 1 M HCl extraction (Ruttenberg, 1992). Since such sequential extraction was not applied in our study, we rely on mass balance equations as a compromise for estimating authigenic $\delta^{18}O_p$ composition:

$$\delta^{18}O_{auth} = (P_{HCl} \times \delta^{18}O_{HCl} - P_{det} \times \delta^{18}O_{det})/(P_{HCl} - P_{det}) \quad (5)$$

$$P_{det} = (P/Al)_{det} \times Al_{bulk} \quad (6)$$

where $\delta^{18}O_{HCl}$ and $\delta^{18}O_{det}$ are the HCl-extractable and detrital $\delta^{18}O_p$ values, respectively, P_{HCl} is the P concentration extracted by 1 M HCl, P_{det} is the detrital P abundance, $(P/Al)_{det}$ represents the P/Al ratio of detrital background, and Al_{bulk} is the bulk Al content.

We assess $\delta^{18}O_{det}$ by compiling available igneous apatite $\delta^{18}O_p$ data (average = 5.3 ± 2.3 ‰; n = 66; Supplementary material). Although local input of phosphate with diverse $\delta^{18}O_{det}$ is possible (Jaisi and Blake, 2010), our discussion will focus on the variation between the $\delta^{18}O_{auth}$ of Mn-rich and Mn-poor samples, rather than the isotopic compositions themselves. A different $\delta^{18}O_{det}$ would systematically shift $\delta^{18}O_{auth}$ to either lower or higher values, thereby not affecting our interpretation. The $(P/Al)_{det}$ ratio is estimated based on the background $(P/Al)_{det}$ of 0.003 (Tan et al., 2021; Shen et al., 2022), which is consistent with the P flux calculation of Canfield et al. (2020).

The derived $\delta^{18}O_{auth}$ compositions vary from 9.4 ‰ to 17.1 ‰ (Fig. 6). Mn carbonates (Mn > 4 wt%) typically have more positive $\delta^{18}O_{auth}$ (average = 14 ‰), while the $\delta^{18}O_{auth}$ values of Mn-poor rocks (Mn < 1 wt%) are relatively lower (average = 10.2 ‰). Bootstrap resampling was performed for the two subsets and the resulting distributions differ significantly (Fig. 8). We consider several factors that may lead to the disparity in $\delta^{18}O_{auth}$ between rocks of different Mn contents. First, the hydrolysis of phosphate from an organic substrate incorporates one or two oxygen atoms from ambient water with large kinetic isotope fractionations, resulting in $\delta^{18}O_p$ ~ 10 ‰ lower than the equilibrium ratio (depending on the substrate and enzymes involved; Liang and Blake, 2006, 2009). As noted above, the Mn^{4+}–Mn^{2+} conversion is accompanied by microbial organic matter degradation. If such a process dominated the $\delta^{18}O_{auth}$ signature, Mn-rich samples should have lighter $\delta^{18}O_{auth}$ as a consequence of intense organic degradation liberating

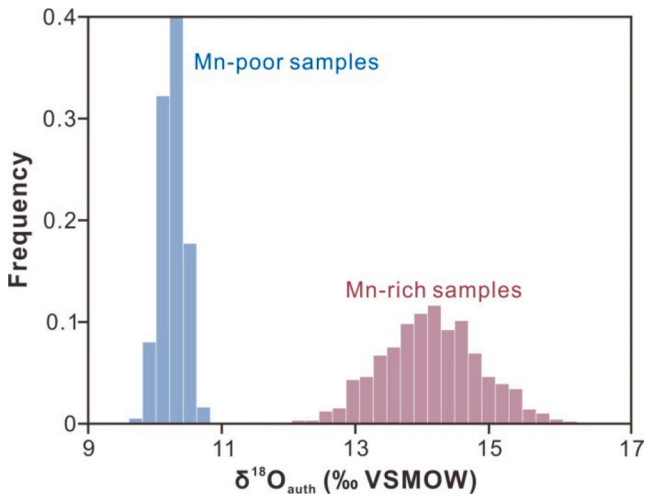

Fig. 8. Frequency distributions of mean $\delta^{18}O_{auth}$ values from bootstrap resampling for Mn-rich and Mn-poor samples (n = 1000).

substantial phosphate with light $\delta^{18}O_p$. However, the $\delta^{18}O_{auth}$ values of the Datangpo Mn carbonates are isotopically heavier than those of Mn-poor shale, hence organic P hydrolysis alone may not account for the $\delta^{18}O_{auth}$ difference.

A second explanation involves various sources of phosphate for apatite precipitation. Apart from organic matter decomposition, phosphate concentration in sedimentary systems can also be regulated by Mn-Fe redox pumping (Dellwig et al., 2010; Ruttenberg, 2014). When Mn-Fe oxides are buried under anoxic conditions, their reduction and dissolution would release large amounts of phosphate, likely facilitating pore-water supersaturation with respect to apatite. Although the fractionation of phosphate oxygen isotopes during Mn oxide adsorption has not been studied, the isotopic effect between Fe oxide-bound P and aqueous phosphate was found to be negligible over geological timescales (Jaisi et al., 2010). Accordingly, a mixture of phosphate from Mn oxide and organic mineralization would result in distinct $\delta^{18}O_p$ signals which could be preserved in apatite phases. For Mn-rich intervals, a higher fraction of phosphate released from Mn oxides tends to imprint a more positive $\delta^{18}O_p$, assuming limited fractionation between Mn oxide-bound and aqueous phosphate as well as a predominant seawater origin of phosphate. On the contrary, samples with less influence of oxide dissolution would exhibit lower $\delta^{18}O_p$ values due to organic enrichments of our samples and the large isotopic offset through organic P hydrolysis. To further test this hypothesis, detailed experimental studies on isotopic fractionation and evaluation of phosphate sources are required.

Third, both laboratory and field studies have proved that equilibrium $\delta^{18}O_p$ can be achieved on the orders of days to weeks via microbial metabolism (Colman et al., 2005; Chang et al., 2021). Assuming extensive oxygen exchange and isotopic equilibrium between phosphate and water, a systematic variation in temperature or $\delta^{18}O_w$ could explain the observed $\delta^{18}O_{auth}$ distribution. Temperature change affects the rate of chemical reactions and metabolic activities. For example, as temperatures rise from 15 to 25 °C, N_2 production by denitrification increases from ~30 to > 100 nmol N/(cm^3 d) (Rysgaard et al., 2004), which might induce large fractionations in N isotopes. However, an investigation of N isotopes from a neighboring site revealed no significant difference among samples with varying Mn contents (Wei et al., 2016). Alternatively, the $\delta^{18}O_{auth}$ offset may indicate contrasting $\delta^{18}O_w$ from which the apatite was formed. Under this hypothesis, the lower $\delta^{18}O_w$ of Mn-poor shales could result from enhanced freshwater input into the basin, whereas the higher $\delta^{18}O_w$ compositions of Mn carbonates point to more seawater-like conditions. Freshwater is distinguished by $\delta^{18}O_w$ signals that are up to 7.7 ‰ lighter than those of coeval seawater. Such an interpretation is in line with analyses of B/Ga ratios for the Datangpo Formation, unveiling elevated salinity at times of Mn-carbonate depositions (Cheng et al., 2021). Manganese stored in basin waters could have been oxidized and deposited as oxides during seawater intrusion. The reduction of Mn oxides after burial enriched Mn^{2+} in pore waters, thus promoting the precipitation of Mn carbonates. Concurrently, authigenic apatite particles formed in the course of inflow events reflect heavier seawater $\delta^{18}O_w$.

To aid the interpretation of our data, we employ a two-endmember mixing PHREEQC model to simulate the precipitation of Mn oxides. The chemistry of basin water used in the calculation was based on major ion compositions of the modern Baltic Sea, where deep waters are sulfidic (Dellwig et al., 2021). Oceanic ingression was set with oxygen concentration of 50 μM, ~20 % of the current seawater oxygen level (Winterer, 2012). As shown in Fig. 9, considerable amounts of Mn oxides would be precipitated when anoxic basin waters account for ~40 % of the total water mass, which imply that the actual difference between the $\delta^{18}O_w$ of seawater and meltwater could be greater than 7.7 ‰. At higher proportions of basin waters, dissolved oxygen imported by marine invasion was rapidly exhausted without the formation of Mn oxide.

5.3. Implications for Mn mineralization

To explore the secular Mn evolution, we present a compilation of Mn concentrations (n = 47,072) from the Sedimentary Geochemistry and Paleoenvironments Project (Farrell et al., 2021), complemented with recently published literature (Sasmaz et al., 2020, 2021; Schier et al., 2020; Gao et al., 2021; Zhang et al., 2022; Dong et al., 2023; Fig. 10a). We note that these samples capture a variety of mineralogy, sedimentation rate, and depositional environment, but our primary intent is to collect all available data to assess the overall trend. We also note that some Archean Mn deposits are not shown in Fig. 10a. Due to extensive metamorphism and supergene modifications, the initial Mn contents of these Archean rocks are unknown. Kuleshov (2011) proposed that economically important Archean Mn ores are mainly hosted within weathered profiles. Moreover, although Mn^{2+} can be oxidized via oxygen-independent pathways, such as anoxygenic photosynthesis and UV photooxidation, its large-scale mineralization would require oxygenated seawater, which is not the case for Archean oceans (Johnson et al., 2016; Robbins et al., 2023).

Our compilation illustrates remarkable Mn enrichments at the early Paleoproterozoic and late Neoproterozoic Eras. Strikingly, similar sequences of geological events occurred in both eras, encompassing

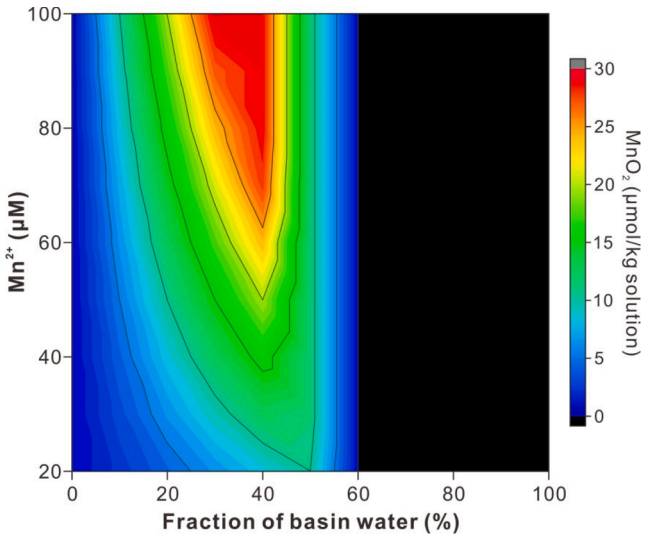

Fig. 9. PHREEQC model displaying the sensitivity of Mn-oxide precipitation to dissolved Mn^{2+} concentration and the mixing ratio between oxygenated seawater and sulfidic basin water.

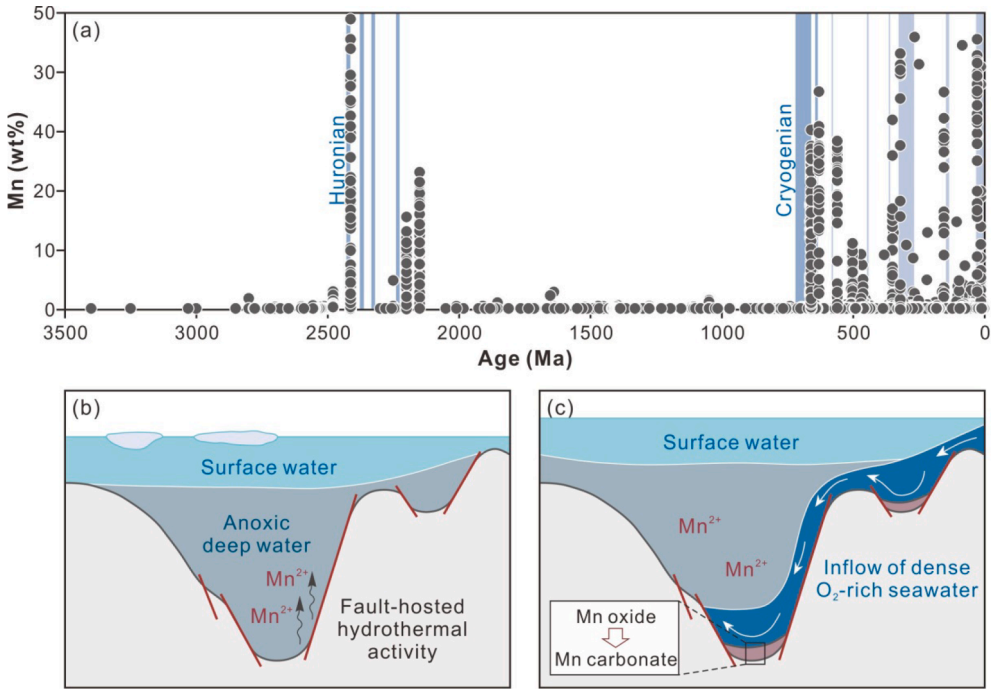

Fig. 10. (a) Sedimentary Mn contents through time. Epochs of global (dark blue) and regional (light blue) glaciations are adopted from Hoffman et al. (2017). (b–c) Schematic illustrations of glacial-related Mn mineralization showing Mn^{2+} enrichment in periods of basin stagnation and Mn-oxide precipitation during seawater intrusions.

continental rifting and breakup, global glaciations, and changes in surface redox states (Roy, 2006). Rift basins developed through the breakup of supercontinents as well as concomitant hydrothermal activities provided an ideal context for the storage of dissolved Mn^{2+}. It could be accumulated to high concentrations under reducing conditions induced by ice-sheet isolation or density stratification (Fig. 10b). In periods of deglaciation, despite the initial injection of meltwater generating a buoyant layer on the ocean surface, the large temperature differences between low latitudes and ice-covered regions can stimulate intense storm systems, thereby accelerating mixing (Higgins and Schrag, 2003; Allen and Hoffman, 2005). In contrast, the newly formed basins with less connection to open oceans were more susceptible to the influence of freshwater. Episodic marine inflows carrying saline and oxygenated seawater into the basin could have oxidized Mn^{2+} and triggered Mn-oxide formation. These oxides were either preserved in their oxide phase or reduced back to Mn^{2+} if the burial conditions were anoxic (Fig. 10c). Further studies on a broad range of Mn deposits worldwide are warranted to confirm the detail of this mechanism.

6. Conclusions

Petrographic and geochemical data from the lower Datangpo Formation document that the Mn carbonates were primarily precipitated as oxides and then transformed to carbonate phases during diagenesis. The differences in $\delta^{18}O_p$ between Mn-rich and Mn-poor rocks can be ascribed to the dominance of phosphate sourced from Mn-Fe oxide or a heavier oxygen isotope value of seawater compared with that of freshwater. We further propose an updated framework for Mn mineralization. In our model, the hydrological condition of the basin was dynamically controlled by the relative fluxes of freshwater and seawater. Episodic marine ingression could have brought oxygenated and saline seawater into the basin, oxidizing Mn^{2+} stored earlier in deep waters. Within anoxic burial environments, the reduction of Mn oxides and paired increase in pore-water Mn^{2+} concentrations led to Mn-carbonate precipitation. A compilation of Mn contents through geological time reveals pronounced Mn enrichments at both ends of the Proterozoic Eon, which might be associated with continental rifting and global glaciation–deglaciation.

CRediT authorship contribution statement

Yuntao Ye: Writing – original draft, Investigation, Funding acquisition, Conceptualization. **Xiaomei Wang:** Writing – review & editing, Funding acquisition, Conceptualization. **Huajian Wang:** Resources, Project administration, Investigation. **Haifeng Fan:** Methodology, Investigation, Funding acquisition. **Zhigang Chen:** Methodology, Investigation. **Qingjun Guo:** Methodology, Investigation. **Ziteng Wang:** Methodology, Investigation. **Chaodong Wu:** Validation, Supervision. **Donald E. Canfield:** Writing – review & editing, Supervision. **Shuichang Zhang:** Supervision, Funding acquisition.

Declaration of competing interest

The authors declare that they have no known competing financial interests or personal relationships that could have appeared to influence the work reported in this paper.

Acknowledgments

This research was funded by the National Natural Science Foundation of China (42225303, 92062221, 42073016, and 42102146), the PetroChina Science and Technology Major Project (2023ZZ0203), the National Key Research and Development Program of China (2021YFA0718200), and the Villum Foundation (16518). We thank Yong Liu at Guiyang University for valuable discussion. Two anonymous reviewers, Associate Editor Ruth E. Blake, and Executive Editor Jeffrey G. Catalano are thanked for their constructive comments and helpful suggestions.

Appendix A. Supplementary material

The attached material includes four tables presenting all the

geochemical data used in the article. Supplementary material to this article can be found online at https://doi.org/10.1016/j.gca.2024.05.021.

References

Ahm, A.-S.-C., Maloof, A.C., Macdonald, F.A., Hoffman, P.F., Bjerrum, C.J., Bold, U., Rose, C.V., Strauss, J.V., Higgins, J.A., 2019. An early diagenetic deglacial origin for basal Ediacaran "cap dolostones". Earth Planet. Sci. Lett. 506, 292–307.

Ai, J., Siljeström, S., Zhong, N., Chen, J., Wang, T., Qiu, N., George, S.C., 2023. Co-existing two distinct formation mechanisms of micro-scale ooid-like manganese carbonates hosted in Cryogenian organic-rich black shales in South China. Precambrian Res. 393, 107091.

Allen, P.A., Hoffman, P.F., 2005. Extreme winds and waves in the aftermath of a Neoproterozoic glaciation. Nature 433, 123–127.

Bau, M., Schmidt, K., Koschinsky, A., Hein, J., Kuhn, T., Usui, A., 2014. Discriminating between different genetic types of marine ferro-manganese crusts and nodules based on rare earth elements and yttrium. Chem. Geol. 381, 1–9.

Blake, R.E., O'Neil, J.R., Surkov, A.V., 2005. Biogeochemical cycling of phosphorus: Insights from oxygen isotope effects of phosphoenzymes. Am. J. Sci. 305, 596–620.

Blake, R.E., Chang, S.J., Lepland, A., 2010. Phosphate oxygen isotopic evidence for a temperate and biologically active Archaean ocean. Nature 464, 1029–1032.

Bowyer, F.T., Krause, A.J., Song, Y., Huang, K.-J., Fu, Y., Shen, B., Li, J., Zhu, X.-K., Kipp, M.A., van Maldegem, L.M., Brocks, J.J., Shields, G.A., Le Hir, G., Mills, B.J.W., Poulton, S.W., 2023. Biological diversification linked to environmental stabilization following the Sturtian Snowball glaciation. Sci. Adv. 9, eadf9999.

Calvert, S.E., Pedersen, T.F., 1996. Sedimentary geochemistry of manganese: Implications for the environment of formation of manganiferous black shales. Econ. Geol. 91, 36–47.

Canfield, D.E., Bjerrum, C.J., Zhang, S., Wang, H., Wang, X., 2020. The modern phosphorus cycle informs interpretations of Mesoproterozoic Era phosphorus dynamics. Earth-Sci. Rev. 208, 103267.

Chang, S.J., Blake, R.E., 2015. Precise calibration of equilibrium oxygen isotope fractionations between dissolved phosphate and water from 3 to 37 °C. Geochim. Cosmochim. Acta 150, 314–329.

Chang, S.J., Blake, R.E., Colman, A.S., 2021. Oxygen isotope exchange rates between phosphate and water catalyzed by inorganic pyrophosphatase: Implications for the biogeochemical cycle of phosphorus. Earth Planet. Sci. Lett. 570, 117071.

Chen, Z.-G., Yin, X.-J., Zhou, Y., 2015. Effects of GC temperature and carrier gas flow rate on on-line oxygen isotope measurement as studied by on-column CO injection. J. Mass Spectrom. 50, 1023–1030.

Cheng, M., Zhang, Z., Algeo, T.J., Liu, S., Liu, X., Wang, H., Chang, B., Jin, C., Pan, W., Cao, M., Li, C., 2021. Hydrological controls on marine chemistry in the Cryogenian Nanhua Basin (South China). Earth-Sci. Rev. 218, 103678.

Colman, A.S., Blake, R.E., Karl, D.M., Fogel, M.L., Turekian, K.K., 2005. Marine phosphate oxygen isotopes and organic matter remineralization in the oceans. Proc. Natl. Acad. Sci. USA 102, 13023–13028.

Dellwig, O., Leipe, T., März, C., Glockzin, M., Pollehne, F., Schnetger, B., Yakushev, E.V., Böttcher, M.E., Brumsack, H.-J., 2010. A new particulate Mn–Fe–P-shuttle at the redoxcline of anoxic basins. Geochem. Cosmochim. Acta 74, 7100–7115.

Dellwig, O., Wegwerth, A., Arz, H.W., 2021. Anatomy of the Major Baltic Inflow in 2014: Impact of manganese and iron shuttling on phosphorus and trace metals in the Gotland Basin. Baltic Sea. Cont. Shelf Res. 223, 104449.

Dong, Z.-G., Peng, Z.-D., Robbins, L.J., Konhauser, K.O., Zhang, B.-L., Zhang, L.-C., Li, J., Li, W.-J., Zhang, L., Wang, C.-L., 2023. Episodic ventilation of euxinic bottom waters triggers the formation of black shale-hosted Mn carbonate deposits. Geochim. Cosmochim. Acta 341, 132–149.

Farrell, Ú.C., Samawi, R., Anjanappa, S., Klykov, R., Adeboye, O.O., Agic, H., Ahm, A.S. C., Boag, T.H., Bowyer, F., Brocks, J.J., Brunoir, T.N., Canfield, D.E., Chen, X., Cheng, M., Clarkson, M.O., Cole, D.B., Cordie, D.R., Crockford, P.W., Cui, H., Dahl, T.W., Mouro, L.D., Dewing, K., Dornbos, S.Q., Drabon, N., Dumoulin, J.A., Emmings, J.F., Endriga, C.R., Fraser, T.A., Gaines, R.R., Gaschnig, R.M., Gibson, T. M., Gilleaudeau, G.J., Gill, B.C., Goldberg, K., Guilbaud, R., Halverson, G.P., Hammarlund, E.U., Hantsoo, K.G., Henderson, M.A., Hodgskiss, M.S.W., Horner, T. J., Husson, J.M., Johnson, B., Kabanov, P., Keller, C.B., Kimmig, J., Kipp, M.A., Knoll, A.H., Kreitsmann, T., Kunzmann, M., Kurzweil, F., LeRoy, M.A., Li, C., Lipp, A. G., Loydell, D.K., Lu, X., Macdonald, F.A., Magnall, J.M., Mänd, K., Mehra, A., Melchin, M.J., Miller, A.J., Mills, N.T., Mwinde, C.N., O'Connell, B., Och, L.M., Ossa Ossa, F., Pagès, A., Paiste, K., Partin, C.A., Peters, S.E., Petrov, P., Playter, T.L., Plaza-Torres, S., Porter, S.M., Poulton, S.W., Pruss, S.B., Richoz, S., Ritzer, S.R., Rooney, A. D., Sahoo, S.K., Schoepfer, S.D., Sclafani, J.A., Shen, Y., Shorttle, O., Slotznick, S.P., Smith, E.F., Spinks, S., Stockey, R.G., Strauss, J.V., Stüeken, E.E., Tecklenburg, S., Thomson, D., Tosca, N.J., Uhlein, G.J., Vizcaíno, M.N., Wang, H., White, T., Wilby, P.R., Woltz, C.R., Wood, R.A., Xiang, L., Yurchenko, I.A., Zhang, T., Planavsky, N.J., Lau, K.V., Johnston, D.T., Sperling, E.A., 2021. The sedimentary geochemistry and paleoenvironments project. Geobiology 19, 545–556.

Faul, K.L., Paytan, A., Delaney, M.L., 2005. Phosphorus distribution in sinking oceanic particulate matter. Mar. Chem. 97, 307–333.

Gao, Z., Zhu, X., Wang, D., Pan, C., Yan, B., Li, J., 2021. Insights into hydrothermal controls and processes leading to the formation of the Late Ediacaran Gaoyan stratiform manganese-carbonate deposit, Southwest China. Ore Geol. Rev. 139, 104524.

Goldhammer, T., Brunner, B., Bernasconi, S.M., Ferdelman, T.G., Zabel, M., 2011. Phosphate oxygen isotopes: Insights into sedimentary phosphorus cycling from the Benguela upwelling system. Geochim. Cosmochim. Acta 75, 3741–3756.

Grossman, E.L., Joachimski, M.M., 2022. Ocean temperatures through the Phanerozoic reassessed. Sci. Rep. 12, 8938.

Havig, J.R., McCormick, M.L., Hamilton, T.L., Kump, L.R., 2015. The behavior of biologically important trace elements across the oxic/euxinic transition of meromictic Fayetteville Green Lake, New York, USA. Geochim. Cosmochim. Acta 165, 389–406.

Herndon, E.M., Havig, J.R., Singer, D.M., McCormick, M.L., Kump, L.R., 2018. Manganese and iron geochemistry in sediments underlying the redox-stratified Fayetteville Green Lake. Geochim. Cosmochim. Acta 231, 50–63.

Higgins, J.A., Schrag, D.P., 2003. Aftermath of a snowball Earth. Geochem., Geophys. Geosyst. 4, 1028.

Hoffman, P.F., Abbot, D.S., Ashkenazy, Y., Benn, D.I., Brocks, J.J., Cohen, P.A., Cox, G. M., Creveling, J.R., Donnadieu, Y., Erwin, D.H., Fairchild, I.J., Ferreira, D., Goodman, J.C., Halverson, G.P., Jansen, M.F., Le Hir, G., Love, G.D., Macdonald, F. A., Maloof, A.C., Partin, C.A., Ramstein, G., Rose, B.E.J., Rose, C.V., Sadler, P.M., Tziperman, E., Voigt, A., Warren, S.G., 2017. Snowball Earth climate dynamics and Cryogenian geology-geobiology. Sci. Adv. 3, e1600983.

Hoffman, P.F., Schrag, D.P., 2002. The snowball Earth hypothesis: testing the limits of global change. Terra Nov. 14, 129–155.

Jaisi, D.P., Blake, R.E., 2010. Tracing sources and cycling of phosphorus in Peru Margin sediments using oxygen isotopes in authigenic and detrital phosphates. Geochim. Cosmochim. Acta 74, 3199–3212.

Jaisi, D.P., Blake, R.E., Kukkadapu, R.K., 2010. Fractionation of oxygen isotopes in phosphate during its interactions with iron oxides. Geochim. Cosmochim. Acta 74, 1309–1319.

Jiang, G., Shi, X., Zhang, S., Wang, Y., Xiao, S., 2011. Stratigraphy and paleogeography of the Ediacaran Doushantuo Formation (ca. 635–551 Ma) in South China. Gondwana Res. 19, 831–849.

Johnson, J.E., Webb, S.M., Ma, C., Fischer, W.W., 2016. Manganese mineralogy and diagenesis in the sedimentary rock record. Geochim. Cosmochim. Acta 173, 210–231.

Kirschvink, J.L., 1992. Late Proterozoic low-latitude global glaciation: the Snowball Earth. In: Schopf, J.W., Klein, C. (Eds.), The Proterozoic Biosphere: A Multidisciplinary Study. Cambridge University Press, pp. 51–52.

Knauth, L.P., Kennedy, M.J., 2009. The late Precambrian greening of the Earth. Nature 460, 728–732.

Koeppenkastrop, D., De Carlo, E.H., 1992. Sorption of rare-earth elements from seawater onto synthetic mineral particles: An experimental approach. Chem. Geol. 95, 251–263.

Kuleshov, V.N., 2011. Manganese deposits: Communication 2. Major epochs and phases of manganese accumulation in the Earth's history. Lithol. Miner. Resour. 46, 546–565.

Lawrence, M.G., Greig, A., Collerson, K.D., Kamber, B.S., 2006. Rare earth element and yttrium variability in South East Queensland waterways. Aquat. Geochemistry 12, 39–72.

Lecuyer, C., Grandjean, P., Sheppard, S.M.F., 1999. Oxygen isotope exchange between dissolved phosphate and water at temperatures ≤135 °C: Inorganic versus biological fractionations. Geochim. Cosmochim. Acta 63, 855–862.

Lenz, C., Jilbert, T., Conley, D.J., Wolthers, M., Slomp, C.P., 2015. Are recent changes in sediment manganese sequestration in the euxinic basins of the Baltic Sea linked to the expansion of hypoxia? Biogeosciences 12, 4875–4894.

Li, C., Love, G.D., Lyons, T.W., Scott, C.T., Feng, L., Huang, J., Chang, H., Zhang, Q., Chu, X., 2012. Evidence for a redox stratified Cryogenian marine basin, Datangpo Formation, South China. Earth Planet. Sci. Lett. 331–332, 246–256.

Liang, Y., Blake, R.E., 2006. Oxygen isotope signature of P_i regeneration from organic compounds by phosphomonoesterases and photooxidation. Geochim. Cosmochim. Acta 70, 3957–3969.

Liang, Y., Blake, R.E., 2007. Oxygen isotope fractionation between apatite and aqueous-phase phosphate: 20–45 °C. Chem. Geol. 238, 121–133.

Liang, Y., Blake, R.E., 2009. Compound- and enzyme-specific phosphodiester hydrolysis mechanisms revealed by $\delta^{18}O$ of dissolved inorganic phosphate: Implications for marine P cycling. Geochim. Cosmochim. Acta 73, 3782–3794.

Liu, M., Li, T., Wei, G., Zhang, F., Chen, J., Li, G., 2023. Redox condition of Cryogenian interglacial seawater in Nanhua Basin constrained by stable tungsten isotopes. Chinese Sci. Bull. 68, 2133–2140 in Chinese with English abstract.

Maynard, J.B., 2010. The chemistry of manganese ores through time: A signal of increasing diversity of Earth-surface environments. Econ. Geol. 105, 535–552.

McLaughlin, K., Sohm, J.A., Cutter, G.A., Lomas, M.W., Paytan, A., 2013. Phosphorus cycling in the Sargasso Sea: Investigation using the oxygen isotopic composition of phosphate, enzyme-labeled fluorescence, and turnover times. Global Biogeochem. Cycles 27, 375–387.

Neumann, T., Christiansen, C., Clasen, S., Emeis, K.C., Kunzendorf, H., 1997. Geochemical records of salt-water inflows into the deep basins of the Baltic Sea. Cont. Shelf Res. 17, 95–115.

Neumann, T., Heiser, U., Leosson, M.A., Kersten, M., 2002. Early diagenetic processes during Mn-carbonate formation: Evidence from the isotopic composition of authigenic Ca-rhodochrosites of the Baltic Sea. Geochim. Cosmochim. Acta 66, 867–879.

Paytan, A., Cade-Menun, B.J., McLaughlin, K., Faul, K.L., 2003. Selective phosphorus regeneration of sinking marine particles: evidence from ^{31}P-NMR. Mar. Chem. 82, 55–70.

Robbins, L.J., Fakhraee, M., Smith, A.J.B., Bishop, B.A., Swanner, E.D., Peacock, C.L., Wang, C.-L., Planavsky, N.J., Reinhard, C.T., Crowe, S.A., Lyons, T.W., 2023.

Manganese oxides, Earth surface oxygenation, and the rise of oxygenic photosynthesis. Earth-Sci. Rev. 239, 104368.
Rooney, A.D., Yang, C., Condon, D.J., Zhu, M., Macdonald, F.A., 2020. U-Pb and Re-Os geochronology tracks stratigraphic condensation in the Sturtian snowball Earth aftermath. Geology 48, 625–629.
Roy, S., 2006. Sedimentary manganese metallogenesis in response to the evolution of the Earth system. Earth-Sci. Rev. 77, 273–305.
Ruttenberg, K.C., 1992. Development of a sequential extraction method for different forms of phosphorus in marine sediments. Limnol. Oceanogr. 37, 1460–1482.
Ruttenberg, K.C., 2014. The global phosphorus cycle. In: Holland, H.D., Turekian, K.K. (Eds.), Treatise on Geochemistry. Elsevier, pp. 499–558.
Rysgaard, S., Glud, R.N., Risgaard-Petersen, N., Dalsgaard, T., 2004. Denitrification and anammox activity in Arctic marine sediments. Limnol. Oceanogr. 49, 1493–1502.
Sasmaz, A., Zagnitko, V.M., Sasmaz, B., 2020. Major, trace and rare earth element (REE) geochemistry of the Oligocene stratiform manganese oxide-hydroxide deposits in the Nikopol. Ukraine. Ore Geol. Rev. 126, 103772.
Sasmaz, A., Sasmaz, B., Hein, J.R., 2021. Geochemical approach to the genesis of the Oligocene-stratiform manganese-oxide deposit, Chiatura (Georgia). Ore Geol. Rev. 128, 103910.
Schier, K., Bau, M., Smith, A.J.B., Beukes, N.J., Coetzee, L.L., Viehmann, S., 2020. Chemical evolution of seawater in the Transvaal Ocean between 2426 Ma (Ongeluk Large Igneous Province) and 2413 Ma ago (Kalahari Manganese Field). Gondwana Res. 88, 373–388.
Shen, W., Zhu, X., Li, J., Yan, B., 2022. Mechanism of organic matter accumulation in black shale of the Datangpo Formation: Insights from paleo-environmental variation during the Cryogenian non-glaciation. Precambrian Res. 383, 106889.
Shields, G.A., 2005. Neoproterozoic cap carbonates: A critical appraisal of existing models and the plumeworld hypothesis. Terra Nov. 17, 299–310.
Shu, L., Yao, J., Wang, B., Faure, M., Charvet, J., Chen, Y., 2021. Neoproterozoic plate tectonic process and Phanerozoic geodynamic evolution of the South China Block. Earth-Sci. Rev. 216, 103596.
Sverjensky, D.A., 1984. Europium redox equilibria in aqueous solution. Earth Planet. Sci. Lett. 67, 70–78.
Tan, Z., Jia, W., Li, J., Yin, L., Wang, S., Wu, J., Song, J., 2021. Geochemistry and molybdenum isotopes of the basal Datangpo Formation: Implications for ocean-redox conditions and organic matter accumulation during the Cryogenian interglaciation. Palaeogeogr. Palaeoclimatol. Palaeoecol. 563, 110169.
Taylor, S.R., McLennan, S.M., 1985. The Continental Crust: Its Composition and Evolution. Blackwell.
Tostevin, R., Shields, G.A., Tarbuck, G.M., He, T., Clarkson, M.O., Wood, R.A., 2016. Effective use of cerium anomalies as a redox proxy in carbonate-dominated marine settings. Chem. Geol. 438, 146–162.
van Maldegem, L.M., Sansjofre, P., Weijers, J.W.H., Wolkenstein, K., Strother, P.K., Wörmer, L., Hefter, J., Nettersheim, B.J., Hoshino, Y., Schouten, S., Sinninghe Damsté, J.S., Nath, N., Griesinger, C., Kuznetsov, N.B., Elie, M., Elvert, M., Tegelaar, E., Gleixner, G., Hallmann, C., 2019. Bisnorgammacerane traces predatory pressure and the persistent rise of algal ecosystems after Snowball Earth. Nat. Commun. 10, 476.
Wang, J., Jacobson, A.D., Sageman, B.B., Hurtgen, M.T., 2023a. Application of the $\delta^{44/40}$Ca-$\delta^{88/86}$Sr multi-proxy to Namibian Marinoan cap carbonates. Geochim. Cosmochim. Acta 353, 13–27.
Wang, J., Li, Z.-X., 2003. History of Neoproterozoic rift basins in South China: implications for Rodinia break-up. Precambrian Res. 122, 141–158.
Wang, Z., Tian, L., Zhao, C., Du, C., Zhang, J., Sun, F., Tekleab, T.Z., Wei, R., Fu, P., Gooddy, D.C., Guo, Q., 2023b. Source partitioning using phosphate oxygen isotopes and multiple models in a large catchment. Water Res. 244, 120382.
Wei, W., Wang, D., Li, D., Ling, H., Chen, X., Wei, G., Zhang, F., Zhu, X., Yan, B., 2016. The marine redox change and nitrogen cycle in the Early Cryogenian interglacial time: Evidence from nitrogen isotopes and Mo contents of the basal Datangpo Formation, northeastern Guizhou, South China. J. Earth Sci. 27, 233–241.
Winterer, E.L., 2012. Pelagic realms. In: Roberts, D.G., Bally, A.W. (Eds.), Regional Geology and Tectonics: Principles of Geologic Analysis. Elsevier, pp. 538–551.
Wittkop, C., Swanner, E.D., Grengs, A., Lambrecht, N., Fakhraee, M., Myrbo, A., Bray, A. W., Poulton, S.W., Katsev, S., 2020. Evaluating a primary carbonate pathway for manganese enrichments in reducing environments. Earth Planet. Sci. Lett. 538, 116201.
Wu, C., Zhang, Z., Xiao, J., Fu, Y., Shao, S., Zheng, C., Yao, J., Xiao, C., 2016. Nanhuan manganese deposits within restricted basins of the southeastern Yangtze Platform, China: Constraints from geological and geochemical evidence. Ore Geol. Rev. 75, 76–99.
Xiao, J., He, J., Yang, H., Wu, C., 2017. Comparison between Datangpo-type manganese ores and modern marine ferromanganese oxyhydroxide precipitates based on rare earth elements. Ore Geol. Rev. 89, 290–308.
Yan, H., Pi, D.H., Jiang, S.Y., Mao, J., Xu, L., Yang, X., Hao, W., Mänd, K., Li, L., Konhauser, K.O., Robbins, L.J., 2022. Mineral paragenesis in Paleozoic manganese ore deposits: Depositional versus post-depositional formation processes. Geochim. Cosmochim. Acta 325, 65–86.
Ye, Y., Wang, H., Zhai, L., Wang, X., Wu, C., Zhang, S., 2018. Contrasting Mo–U enrichments of the basal Datangpo Formation in South China: Implications for the Cryogenian interglacial ocean redox. Precambrian Res. 315, 66–74.
Ye, Y., Wang, X., Wang, H., Fan, H., Chen, Z., Guo, Q., Wang, Z., Wu, C., Canfield, D.E., Zhang, S., 2024a. Phosphate oxygen isotopes constrain Mesoproterozoic marine temperatures and the paucity of phosphorite. Chem. Geol. 644, 121831.
Ye, Y., Wang, X., Wang, H., Wu, C., Zhang, S., 2024b. Exploring climate variability during the Marinoan glaciation: A study of black shale geochemistry. Gondwana Res. 128, 315–324.
Yu, W., Algeo, T.J., Du, Y., Maynard, B., Guo, H., Zhou, Q., Peng, T., Wang, P., Yuan, L., 2016. Genesis of Cryogenian Datangpo manganese deposit: Hydrothermal influence and episodic post-glacial ventilation of Nanhua Basin, South China. Palaeogeogr. Palaeoclimatol. Palaeoecol. 459, 321–337.
Yu, W., Algeo, T.J., Du, Y., Zhou, Q., Wang, P., Xu, Y., Yuan, L., Pan, W., 2017. Newly discovered Sturtian cap carbonate in the Nanhua Basin, South China. Precambrian Res. 293, 112–130.
Zhang, B., Cao, J., Hu, K., Liao, Z., Zhang, Y., Shi, C., 2022. Microbially-mediated Mn redox cycling and Mn carbonate precipitation in the Marinoan glacial aftermath, South China. Glob. Planet. Change 217, 103950.
Zhang, S., Jiang, G., Han, Y., 2008. The age of the Nantuo Formation and Nantuo glaciation in South China. Terra Nov. 20, 289–294.
Zhang, J., Nozaki, Y., 1996. Rare earth elements and yttrium in seawater: ICP-MS determinations in the East Caroline, Coral Sea, and South Fiji basins of the western South Pacific Ocean. Geochim. Cosmochim. Acta 60, 4631–4644.
Zhang, F., Zhu, X., Yan, B., Kendall, B., Peng, X., Li, J., Algeo, T.J., Romaniello, S., 2015. Oxygenation of a Cryogenian ocean (Nanhua Basin, South China) revealed by pyrite Fe isotope compositions. Earth Planet. Sci. Lett. 429, 11–19.
Zhao, M., Blake, R.E., Liang, Y., Ruf, D.D., Jaisi, D.P., Chang, S.J., Planavsky, N.J., 2021. Oxygen isotopic fingerprints on the phosphorus cycle within the deep subseafloor biosphere. Geochim. Cosmochim. Acta 310, 169–186.
Zhou, C., Huyskens, M.H., Lang, X., Xiao, S., Yin, Q.Z., 2019. Calibrating the terminations of Cryogenian global glaciations. Geology 47, 251–254.